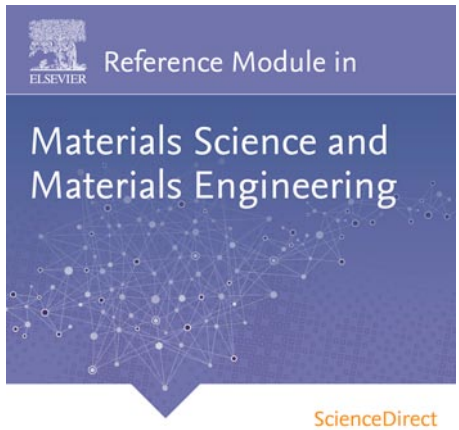

Ahuja B.L., and Dashora A., Compton Scattering. In: Saleem Hashmi (editor-in-chief), Reference Module in Materials Science and Materials Engineering. Oxford: Elsevier; 2016. pp. 1-8.

ISBN: 978-0-12-803581-8

Compton Scattering ☆

BL Ahuja, M.L. Sukhadia University, Udaipur, India
A Dashora, UM-DAE Centre for Excellence in Basic Sciences, Mumbai, India

1 Introduction

Compton effect which was invented by Arthur Holly Compton (Compton, 1923a,b) was a milestone in the development of quantum mechanics. In 1929, DuMond and collaborators (DuMond, 1929) firstly explained the shape of Compton profile of beryllium within the Fermi–Dirac statistics. After that a couple of basic studies on Compton profiles and the electron momentum densities were performed in the 1930s (DuMond and Kirkpatrick, 1930). With the development of new generation of photon detectors, this technique was re-established in the mid-1960s. Several reviews on development of this technique are available in literature (Williams, 1977; Cooper, 1985; Lovesey and Collins, 1995; Cooper *et al.*, 2004; Schülke, 2007; Ahuja, 2010). With the advent of third generation synchrotron radiation (SR) sources along with the further improvement in the detector technology, Compton scattering (CS) is now established as a well recognized tool to study electronic properties of variety of materials. Even CS is being employed to study the magnetic behavior of materials using circularly polarized SRs.

Other experimental methodologies like de Haas–van Alphen (dHvA) effect, 2-Dimensional angular correlation of annihilation radiation (2D-ACAR) and angle resolved photoemission have limitations like requirement of ultra-high vacuum, low temperature, and very high purity of samples. In contrast, CS does not require low temperature and from an experimental point of view it is not sensitive to lattice defects. Further, unlike de Haas–van effect, CS technique does not require a long electron mean free path.

2 Kinematics

CS of photons from bound electrons wherein an electron is ejected from the atom is shown in **Figure 1(a)**. The energy and momentum of the incident and scattered photon and the initially bound and escaped electron remains conserve in the scattering process. If ω_1 ($\mathbf{k}_1$) is energy (momentum) of incident photon and ω_2 ($\mathbf{k}_2$) is that of scattered photons and if scattered photon transfers energy $\Delta\omega$ to the target electron then the modulus of transferred momentum is given by

$$p = \frac{1}{c}\sqrt{\omega_1^2 + \omega_2^2 - 2\omega_1\omega_2\cos\theta} \qquad [1]$$

where θ is the angle between $\mathbf{k}_1$ and $\mathbf{k}_2$ (the wave vectors for incident and scattered photons). The scattering vector can be defined as $\mathbf{k}=\mathbf{k}_1-\mathbf{k}_2$. In the CS process, energy transferred ($\Delta\omega$) can be given as,

$$\Delta\omega = \frac{k^2}{2m_e} + \frac{\mathbf{p}_1\cdot\mathbf{k}}{m_e} \qquad [2]$$

In eqn [2], the first term is known as recoil-term while the second term is known as the Doppler term. The recoil-term describes the kinematics of the inelastic X-ray scattering process. It relies upon the experimental parameters and corresponds to a mean value of energy transfer (the Compton shift). The Doppler term depends on the initial state of the electron at the time of scattering and the

☆*Change History*: June 2015. B.L. Ahuja and A Dashora have rewritten the article. All the figures are new.

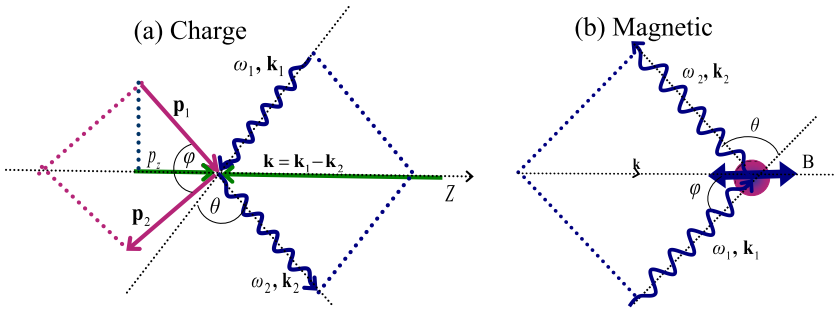

Figure 1 Schematic diagram of inelastic (a) charge and (b) magnetic Compton scattering with incoming photon of energy ω_1, wave vector $\mathbf{k}_1$ scattered through an angle θ from a moving electron with initial momentum $\mathbf{p}_1$. The subscript 2 refers to 'after scattering' process. In (b) the direction of applied magnetic field B is along or opposite to the scattering vector $\mathbf{k}$. (We have used atomic units, e=m=$\hbar$=1.)

broadening of the line spectrum of scattered X-rays due to the initial momentum $\mathbf{p}_1$ (non-zero) of the target electron. In this process, impulse approximation (IA) condition wherein it is assumed that the energy transferred to the electron is much greater than its binding energy holds good.

In case the incident radiation has some degree of circular polarization and ferro- or ferri-magnetic sample is placed in a fixed magnetic field, then by varying the direction of external magnetic field (Figure 1(b)) one can obtain Compton data for spin-up and spin-down electrons. The subtraction of spin-down data from spin-up data leads to the magnetic Compton profiles (MCPs). Due to its incoherent nature, the MCP is sensitive to the spin moment of the magnetic materials.

3 Basic Aspects of Compton Profile

Experimentally, in charge (normal) CS, we fix the direction of the incident photons and measure the energy distribution of the scattered photons at the largest possible scattering angle θ (close to 180°) to increase the magnitude of the scattering vector $\mathbf{k}$.

The CS experiments can be related to electronic structure calculations through the scattering cross-section. Within IA, a relationship between the Compton double differential scattering cross-section and Compton profile $J(p_z)$ is given below,

$$\frac{\mathrm{d}^2\sigma}{\mathrm{d}\Omega \mathrm{d}\omega_2} = C(\omega_1, \omega_2, \theta, p_z) J(p_z) \qquad [3]$$

where the function

$$C(\omega_1, \omega_2, \theta, p_z) = \left(\frac{e}{4\pi mc}\right)^4 \left[\frac{\omega_1\left(1+\frac{p_z}{mc}\right)}{\omega_2\left(1-\frac{p_z}{mc}\right)} + \frac{\omega_2\left(1-\frac{p_z}{mc}\right)}{\omega_1\left(1+\frac{p_z}{mc}\right)}\right] * B$$

with

$$B = \left[\frac{\omega_2 mc}{2\omega_1(\omega_1^2 + \omega_2^2 - 2\omega_1\omega_2\cos\phi)^{1/2} + \frac{p_z(\omega_1-\omega_2)}{mc}}\right]$$

and

$$p_z = \frac{\vec{\mathbf{k}}.\vec{\mathbf{p}}_1}{|\mathbf{k}|}$$

The quantity 'C' which is a function of ω_1, ω_2, θ, and the electron momentum component (p_z) has been calculated for relativistic energies by Eisenberger and Reed (1974) for scattering angle 180° and by Ribberfors (1975a,b) for all scattering angles.

Theoretically $J(p_z)$ can be expressed as

$$J(p_z) = \int_{px}\int_{py} \rho(\vec{p})\, \mathrm{d}p_x \mathrm{d}p_y \qquad [4]$$

where $\rho(p_z)$ is the electron momentum density which can be derived from the Fourier transform of real space wave function.

The Compton profile has the property that

$$\int_{-\infty}^{+\infty} J(p_z)\,\mathrm{d}p_z = N \qquad [5]$$

N is the number of electrons contributing in Compton phenomenon, which is used to normalize theoretical and experimental Compton profile.

In case of scattering of circularly polarized photons with electron, Lipps and Tolhoek (1954) have reported formulae for cross-section describing all possible combinations of photon and electron polarization for CS from a stationary electron. According to Lipps and Tolhoek (1954), $\mathrm{d}\sigma/\mathrm{d}\omega$ can be given as,

$$\frac{\mathrm{d}\sigma}{\mathrm{d}\omega} = \frac{r_e^2}{2}\left(\frac{k_2^2}{k_1^2}\right)\left[1-\cos^2\theta + P_l\sin^2\theta + \frac{(k_1-k_2)}{mc}(1-\cos\theta) + (\cos\theta-1)P_c S\frac{(k_1\cos\theta+k_2)}{mc}\right] \qquad [6]$$

where S is the Stokes parameter for the spin polarization of the electron and P_l and P_c are the degrees of linear and circular polarizations, respectively, of the incoming photons.

Equation [6] consists of components which are independent of the polarization of the electron (charge term) and other terms which linearly depend on the spin of the system (magnetic/spin term). S can be written in terms of a unit vector, $\hat{\sigma}$, involving the direction of the spin polarization and the magnitude of the spin polarization of the system. The double differential cross-section (DDC) for a system of moving electrons can be written as,

$$\frac{\mathrm{d}^2\sigma}{\mathrm{d}\Omega\mathrm{d}\omega_2} = \frac{r_e^2}{2}\left(\frac{k_2^2}{k_1^2}\right)\left[\left(1+\cos^2\theta + P_l\sin^2\theta + \frac{(k_1-k_2)}{mc}(1-\cos\theta)\right)J(p_z) + (\cos\theta-1)P_c\hat{\sigma}\frac{(\mathbf{k}_1\cos\theta+\mathbf{k}_2)}{mc}J_{\mathrm{mag}}(p_z)\right] \qquad [7]$$

A quick inspection of eqn [7] shows that the magnetic term (which involves multiplication of $J_{\mathrm{mag}}(p_z)$ known as MCP) can be isolated by changing its sign either by reversing the hand of polarization of the incident photon beam (by flipping P_c), or by changing the direction of $\hat{\sigma}$ which is done by reversing the direction of the spin vector with an external magnetic field ($\hat{\sigma} = \pm 1$). Here J_{mag} (p_z) can be deduced from the DDC by subtracting DDC of spin-down ($\downarrow$) from that of spin-up ($\uparrow$) contribution. Mathematically,

$$\left(\frac{\mathrm{d}^2\sigma}{\mathrm{d}\Omega\mathrm{d}\omega_2}\right)^{\mathrm{mag}} = \left(\frac{\mathrm{d}^2\sigma}{\mathrm{d}\Omega d\omega_2}\right)^{\uparrow} - \left(\frac{\mathrm{d}^2\sigma}{\mathrm{d}\Omega\mathrm{d}\omega_2}\right)^{\downarrow} \propto J_{\mathrm{mag}}(p_z) \qquad [8]$$

Theoretically, one can derive MCP, J_{mag} (p_z), as

$$J_{\mathrm{mag}}(p_z) = \iint \left[\rho^{\uparrow}(\mathbf{p}) - \rho^{\downarrow}(\mathbf{p})\right]\mathrm{d}p_x\mathrm{d}p_y \qquad [9]$$

where $\rho^{\uparrow}(\mathbf{p})[\rho^{\downarrow}(\mathbf{p})]$ denote momentum density with the majority [minority] spin. From eqn [9], it can be noted that MCP is described by the double integral of spin momentum density. The area under the MCP is proportional to spin magnetic moment (μ) per formula unit,

$$\int_{-\infty}^{\infty} J_{\mathrm{mag}}(p_z)\mathrm{d}p_z = \mu \text{ (in Bohr magnetons)} \qquad [10]$$

Usually, due to experimental limitations, the experimental spin momentum density can be determined by measuring the spectrum of scattered radiation by reversing sample magnetization. A subtraction of spin-up and down cross-sections shows a weak signal which is basically raw MCP. The ratio of the magnetic signal ($I^{\uparrow} - I^{\downarrow}$), isolated by this procedure, to the charge signal ($I^{\uparrow} + I^{\downarrow}$) leads to magnetic effect, R. Mathematical formulation for R is as follows,

$$\begin{aligned} R = \frac{I^{\uparrow}-I^{\downarrow}}{I^{\uparrow}+I^{\downarrow}} &= \frac{(\cos\theta-1)P_c\hat{\sigma}\frac{(\mathbf{k}_1\cos\theta+\mathbf{k}_2)}{mc}}{1+\cos^2\theta+P_l\sin^2\theta+\frac{(\mathbf{k}_1-\mathbf{k}_2)}{mc}(1-\cos\theta)}\frac{\mu}{N_1} \\ &= \frac{(\cos\theta-1)P_c\frac{\omega_1}{mc^2}\left[\cos\theta\cos\varphi+\frac{\omega_2}{\omega_1}\cos(\theta+\varphi)\right]}{1+\cos^2\theta+P_l\sin^2\theta+\frac{(\omega_1-\omega_2)}{mc^2}(1-\cos\theta)}\frac{\mu}{N_1} \end{aligned} \qquad (11)$$

In eqn [11], N_1 is total number of electrons in specimen and φ is the angle between the incident photon direction and the magnetic field. In such experiments, the experimental parameters are optimized to get maximum value of R which is essential to get high statistical accuracy in $J_{\mathrm{mag}}(p_z)$ during a short period of exposure of specimen.

4 Instrumentation and Data Reduction

The first synchrotron based Compton spectrometer consisting of combination of a crystal analyzer and a position sensitive detector was constructed by Loupias and Petiau (1980) at LURE-DC1 (Orsay, France). Although the incident X-ray energy was about 15 keV, the highest momentum resolution of 0.15 a.u. (where 1 a.u. $= 1.9929 \times 10^{-24}$ Kg m s^{-1}) was achieved. Shiotani *et al.* (1989) have reported design of a high resolution spectrometer for CS measurements using 29.5 keV SRs from the vertical wiggler inserted in the 2.5 GeV storage ring of the Photon Factory at Tsukuba, Japan. Due to limitations of availability of SR sources, use of SR in such measurements was found to be very limited.

After development of semiconductor detectors, X-ray scattering was replaced by γ-ray CS which overcame many limitations of X-ray scattering (low energy, multi-energy input). A γ-ray source for CS can have a high specific activity, a long half life, monochromatic γ-ray emission in the desired range 40–700 keV and clean space in the Compton profile region. Felsteiner *et al.* (1970) measured first quantitative Compton profile of graphite using 300 mCi ^{241}Am source (energy = 59.54 keV and half life = 432.2 years). The high energy sources such as ^{123m}Te (energy = 159 keV and half life = 109 days) (Holt *et al.*, 1979) and ^{198}Au (energy = 412 keV and half life = 2.7 days) have advantage in terms of resolution, but more importantly the reduced photoelectric absorption cross-section at higher energies. Using annular ^{241}Am sources, Cooper *et al.* (1978) and Manninen and Paakkari (1978) developed Compton spectrometers with resolution of 0.6 a.u. Chang *et al.* (1991) employed 95 Ci ^{137}Cs radioisotope (half life = 30.2 years) to commission a high energy Compton spectrometer. Further, a Compton spectrometer which employs either 662 keV or 412 keV γ-rays was designed and built by Andrejczuk *et al.* (1993). Ahuja *et al.* (2006, 2007) have designed 20 Ci ^{137}Cs and 100 mCi ^{241}Am Compton spectrometers and suggested unique designs to employ relatively low intensity sources. Schematics of 20 Ci ^{137}Cs and 100 mCi ^{241}Am Compton spectrometers (Ahuja *et al.*, 2006, 2007) are given in **Figures 2** and **3**, respectively.

Magnetic Compton scattering (MCS) was introduced in 1970 (Platzman and Tzoar, 1970) and verified experimentally in 1976 (Sakai and Ono, 1976) using circularly polarized radiations emitted by ^{57}Co source kept at mK temperature. Difficulty in getting low temperature and extremely poor statistics prevented the effective use of γ-rays in MCS experiments. There have been renewed interest in the MCS after operation of third generation SR sources. The European Synchrotron Radiation Facility (ESRF) in Grenoble was the first of the third generation hard X-ray sources which facilitated beamline for MCS in 1994. The SPring-8, Japan SR source provides the highest flux and highest energy in the world which is very useful in ongoing MCP measurements.

In CS experiments, one has to extract-out an accurate $J(p_z)$ from the measured DDC-section spectra. To deduce the true $J(p_z)$, we need to correct the raw data for several systematic corrections. These corrections which are governed by the geometry of spectrometer, sample properties, and the source energy are (1) background, (2) deconvolution, (3) absorption of photons in the sample, (4) detector efficiency, (5) CS cross-section, and (6) multiple scattering, etc. Similarly, to obtain true $J_{mag}(p_z)$, the raw data are corrected for beam decay, background, energy dependence of the absorption of the photons in the sample, energy dependence of the magnetic Compton cross-section and multiple scattering. Necessity of detector efficiency correction depends upon the energy of scattered photons.

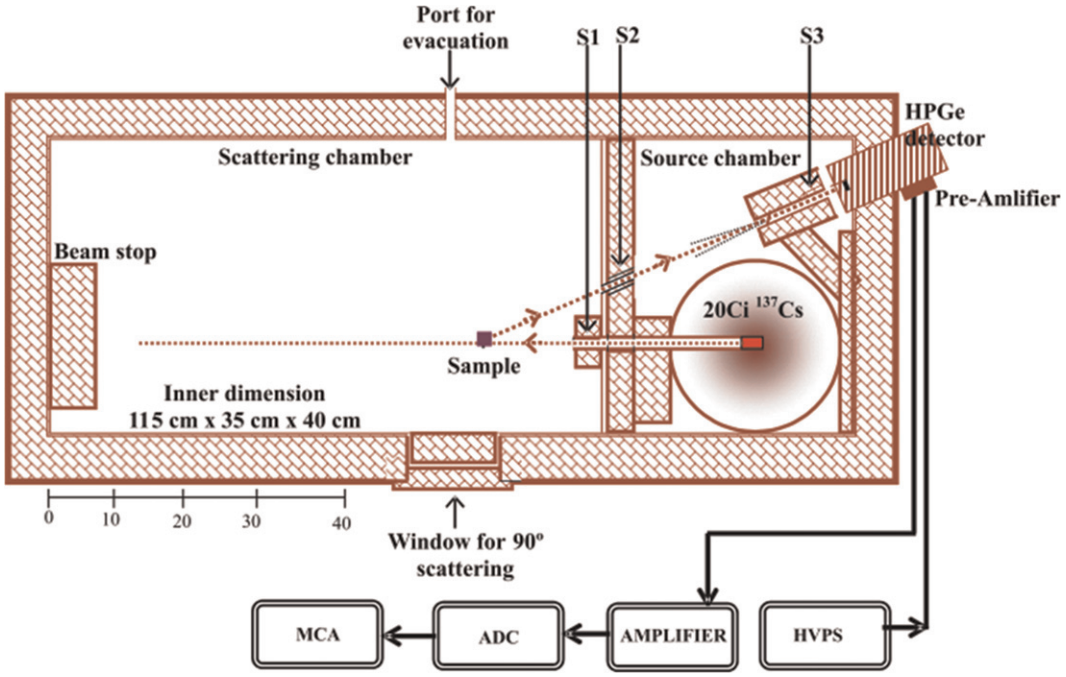

Figure 2 Layout of ^{137}Cs Compton spectrometer. The regions marked with small bricks show the interlocked lead shielding to save the human beings. S1, S2, and S3 represent the collimating slits.

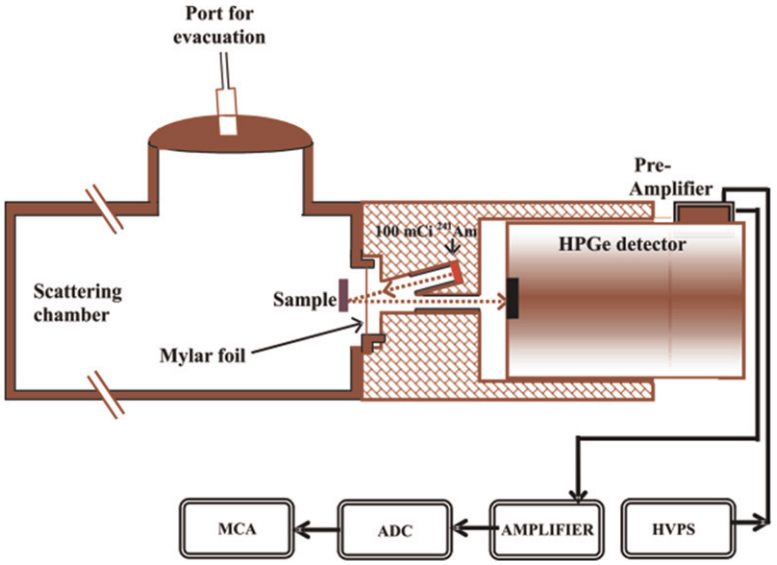

Figure 3 Schematic diagram of 100 mCi ^{241}Am Compton spectrometer. The scattering chamber is made of hollow brass pipe (10 cm diameter) while the ^{241}Am source is fixed in a cylindrical lead block.

5 Applications

5.1 Study of Charge Transfer in Alloys

Quantitative estimation of charge transfer in condensed matter physics is frustratingly difficult particularly in case of disordered alloys. In such alloys, CS is a very useful technique to deduce the charge reorganization. In a representative example, $J(p_z)$ of Cr–Al alloy has been analyzed in terms of individual $J(p_z)$ contributions of the constituents as seen in (**Figure 4**; Dashora and Ahuja, 2010). The key point in deducing the charge reorganization is that the momentum distribution is built from the superposition of the contribution from different electrons of the constituents. In comparison to Al, the valence band Compton profile of Cr extends to higher momentum. It is seen that the half widths of valence electron Compton profiles of Cr and Al differ by more than 40%. Therefore, the valence band Compton profiles of the alloy can be synthesized using the valence profiles of the constituent elements using the least square curve fitting. The following relation is used in the fitting of individual experimental valence band profiles of Cr and Al to the valence experimental Compton profile of alloy,

$$E = \sum_{p_z=0}^{7.0\ \text{a.u.}} \left[J_{\text{Alloy}}^{\text{Val.Expt}}(p_z) - m\, J_{\text{Cr}}^{\text{Val.Expt}}(p_z) - n\, J_{\text{Al}}^{\text{Val.Expt}}(p_z) \right]^2 \quad [12]$$

The weight factors m and n are derived for the best fit to the alloy valence Compton profile. In order to compute the valence experimental Compton profile of Cr–Al alloy and Cr and Al, we have subtracted the corresponding convoluted free atom core profile (Biggs *et al.*, 1975) from the total experimental profiles. **Figure 4** depicts the experimental valence Compton profile of alloy, its decomposition into the Cr and Al valence profiles and the best fitted Compton profile. The number of electrons on the individual sites is equal to area under the component profile. Within the superposition approximation, valence electrons of Al and Cr in the fractional composition of alloy are expected to be 0.60 and 4.80 e^-, respectively. From the area under curve of fitted Al and Cr profiles (**Figure 4**), it is seen that after formation of alloy, occupancies of Al and Cr comes out to be 0.80 and 4.64 e^-, respectively. Therefore, a charge transfer from Cr to Al is predicted as 0.18 ± 0.04 e^- (Dashora and Ahuja, 2010) which is in good agreement with the X-ray photoemission spectroscopy data of Jablonska *et al.* (1984). In the inset of **Figure 4**, the Compton profiles of alloy and constituted elements are computed using spin polarized relativistic Korringa–Kohn–Rostoker (SPR–KKR) scheme (Ebert, 2000) which also shows almost a similar charge transfer in the studied Cr–Al alloy.

5.2 Nature of Bonding

To compare the nature of bonding between isoelectronic MoS_2 and $MoTe_2$ layered compounds, the experimental equal-valence-electron-density (EVED) profiles (on p_z/p_F scale, where p_F is the Fermi momentum) have been plotted in **Figure 5**. The similarity in the EVED profiles shows the similarity in wave function for bonding electrons in isoelectronic materials, if written as a function of r/a (a being the lattice parameter). Hence relative nature of bonding in isovalent compounds can be judged using amplitude of

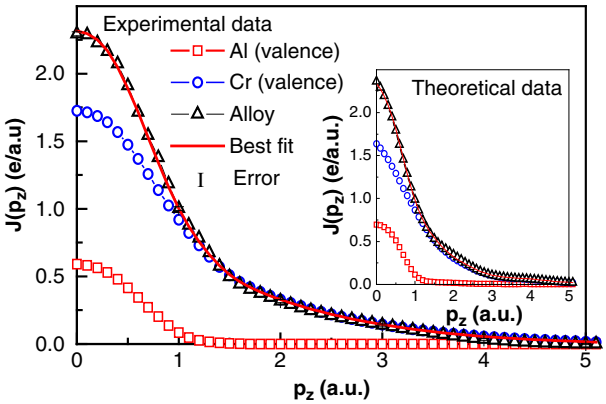

Figure 4 Decomposition of experimental valence Compton profiles of $Cu_{0.8}Al_{0.2}$ into valence band Compton profiles of Al and Cu. In the inset, decomposition is done using theoretically (SPR–KKR) computed valence Compton profiles of alloy and constituted elements.

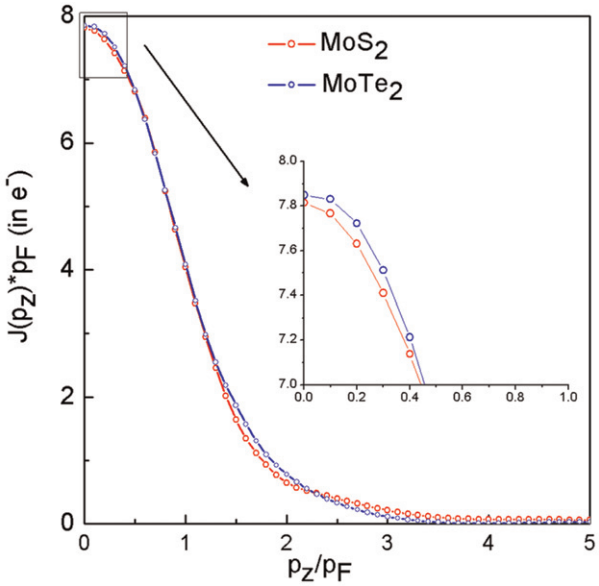

Figure 5 Equal-valence-electron-density (EVED) experimental profiles on (p_z/p_F scale) of MoS_2 and $MoTe_2$. Marked region is figure is enlarged in the inset.

momentum density at $p_z/p_F=0$. From Figure 5, $J(0)$ value of $MoTe_2$ is found to be slightly higher than that of MoS_2 suggesting more localization of charge or say more covalent nature in $MoTe_2$ in the bonding direction (Heda *et al.*, 2010).

5.3 Applicability to Accurately Determine Small Spin Moments

Magnetic CS can be used to determine small spin moments of ferri-magnetic materials and also to deduce site specific moments of the constituents. The spin moment at 85 and 300 K (magnetic field 2.5 T) for $LaFe_{0.6}Ni_{0.4}O_3$ from MCS experiment was obtained as 0.17 ± 0.02 and 0.16 ± 0.02 μ_B/f.u. which is very close to the measured magnetization data which gives total (spin + orbital) magnetic moment as 0.16 and 0.15 μ_B/f.u., respectively (Dashora *et al.*, 2013). In **Figures 6(a)** and **6(b)**, the experimental MCPs are decomposed into constituent profiles (Fe, Ni and diffuse electrons) to determine the site specific spin moments. For this fitting, experimental MCPs of Fe and Hartree–Fock free atom profiles (Biggs *et al.*, 1975) of Ni 3d electrons were considered. To account the contribution of itinerant (diffuse) electrons, full width at half maximum (FWHM) of 1.5 a.u. (which corresponds to the FWHM of free electron Compton profiles of La 6s, 5d; Ni 4s; and O 2s, 2p electrons) is used. To incorporate the effect of experimental resolution (0.4 a.u.), all the theoretical profiles were convoluted with a Gaussian FWHM of 0.4 a.u. Since the area under each component profile gives the contribution of spin moment per formula unit at that site, it is seen that the Fe site gives the dominant (although small) contribution to the total magnetic moment. It turns out that the Ni 3d electrons are coupled

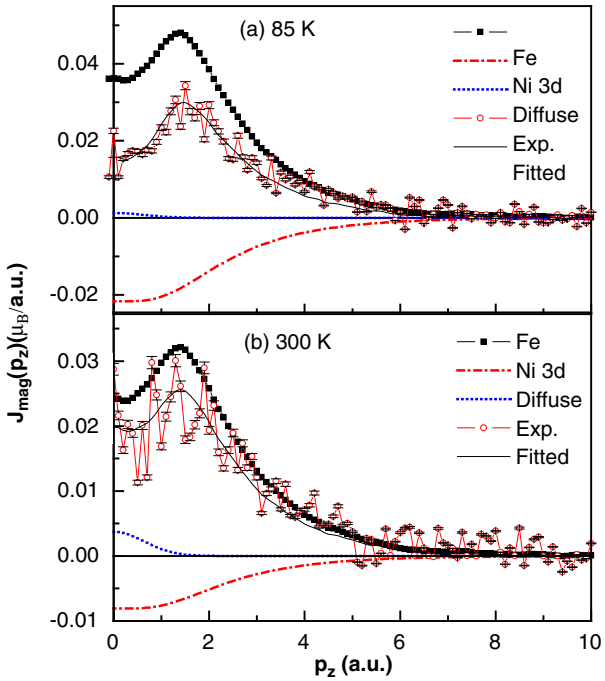

Figure 6 Experimental magnetic Compton profiles of $LaFe_{0.6}Ni_{0.4}O_3$ at (a) 85 and (b) 300 K. Experimental MCPs are also decomposed into constituent profiles to deduce the spin moments at different sites (constituents).

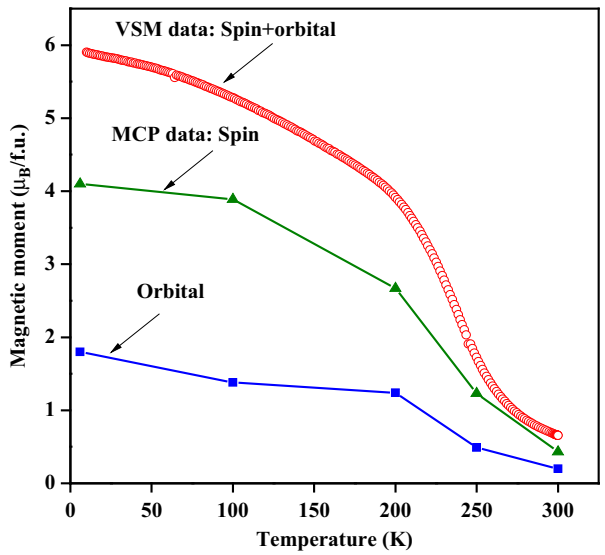

Figure 7 Temperature dependent total (VSM data), spin (MCP data), and orbital (VSM–MCP) magnetic moment in $TbCo_2$. Solid lines are drawn to guide the eyes.

anti-ferromagnetically to Fe spin moment. The present splitting demonstrates a peculiar applicability of MCS in separating a small contribution of spin moment arising from the different sites (Dashora *et al.*, 2013).

5.4 Estimation of Accurate Orbital Magnetic Moment

As estimated earlier, MCS provides only the information about spin magnetic moment of the material. If we compare MCS data with magnetization data which gives total (spin + orbital) magnetic moment than the contribution of orbital magnetic moment can be deduced. In **Figure 7**, the values of total spin moment of $TbCo_2$ at different temperatures derived from MCS data are plotted (Ahuja *et al.*, 2015). In order to determine the orbital moment, the magnetization measurements from 6 to 300 K (2.5 T external

magnetic field) using vibrating sample magnetometer (VSM) are also shown in **Figure 7**. At 6 K, the orbital moment for $TbCo_2$ is found to be $1.80 \pm 0.03\ \mu_B$/f.u. It is interesting to note that with increase in temperature ($6 \rightarrow 300$ K), ratio of orbital to spin moments decreases from 43.9 to 35.0%. The experimental values are also found to be in agreement with the theoretical data derived using full potential linearized augmented plane wave (FP-LAPW) approach (Blaha *et al.*, 2012). The computed value of ratio of orbital to spin moments (38%) is in tune with the present experimental values. From FP-LAPW calculations it is concluded that the major contribution to orbital magnetic moment is due to the Tb site with a small contribution (17%) of Co. The computed orbital moment at Co site is also anti-parallel to the Tb orbital moment, like their spin moments as observed from MCP investigations.

References

Ahuja, B.L. (Ed.), 2010. Recent Trends in Radiation Physics Research. India: Himanshu Publications.

Ahuja, B.L., Mund, H.S., Sahariya, J., *et al.*, 2015. Temperature dependent spin and orbital magnetization in $TbCo_2$: Magnetic Compton scattering and first-principles study. Journal of Alloys and Compounds 633, 430–434.

Ahuja, B.L., Sharma, M., Mathur, S., 2006. Anisotropy in the momentum density of tantalum. Nuclear Instruments and Methods in Physics Research Section B 244, 419–426.

Ahuja, B.L., Sharma, V., Rathor, A., Jani, A.R., Sharma, B.K., 2007. Electronic structure of rhodium using Compton profiles: Experiment and theory. Nuclear Instruments and Methods in Physics Research Section B 262, 391–398.

Andrejczuk, A., Żukowski, E., Dobrzyński, L., Cooper, M.J., 1993. A spectrometer for Compton scattering studies of heavy elements and the problem of bremsstrahlung background. Nuclear Instruments and Methods in Physics Research Section A 337, 133–144.

Biggs, F., Mendelsohn, L.B., Mann, J.B., 1975. Hartree–Fock Compton profiles for the elements. Atomic Data and Nuclear Data Tables 16, 201–308.

Blaha, P., Schwarz, K., Madsen, G.K.H., Kvasnicka, D., Luitz, J., 2012. Wien2k Code, an Augmented Plane Wave Plus Local Orbitals Program for Calculating Crystal Properties. Vienna, Austria: Vienna University of Technology.

Chang, C.N., Lee, S.B., Chen, C.C., 1991. Compton profiles of silver with 662 keV γ-rays. Journal of the Physical Society of Japan 60, 4253–4264.

Compton, A.H., 1923a. A quantum theory of the scattering of X-rays by light elements. Physical Review 21, 483–502.

Compton, A.H., 1923b. The spectrum of scattered X-rays. Physical Review 22, 409–413.

Cooper, M.J., 1985. Compton scattering and electron momentum determination. Reports on Progress in Physics 48, 415–481.

Cooper, M.J., Holt, R.S., DuBard, J.L., 1978. A ^{241}Am spectrometer for Compton scattering studies. Journal of Physics E: Scientific Instruments 11, 1145–1148.

Cooper, M.J., Mijnarends, P.E., Shiotani, N., Sakai, N., Bansil, A., 2004. X-ray Compton Scattering. New York: Oxford Science Publications, Oxford University Press.

Dashora, A., Ahuja, B.L., 2010. Electronic structure of Cr-Al alloy: Theory and experiment. Journal of Alloys and Compounds 501, 1–5.

Dashora, A., Sahariya, J., Choudhary, R.J., *et al.*, 2013. Feasibility of magnetic Compton scattering in measurement of small spin moments: A study of $LaFe_{1-x}Ni_xO_3$ ($x=0.4$ and 0.5). Applied Physics Letters 02.142403-1-4.

DuMond, J.W.M., 1929. Compton modified line structure and its relation to the electron theory of solid bodies. Physical Review 33, 643–658.

DuMond, J.W.M., Kirkpatrick, H.A., 1930. The multiple crystal X-ray spectrograph. Review of Scientific Instruments 1, 88–105.

Ebert, H., 2000. Band structure calculations for magnetic solids-formulations and applications. In: Dressé (Ed.), Electronic Structure and Physical Properties of Solid. Berlin: Springer, pp. 191–246.

Eisenberger, P., Reed, W.A., 1974. Relationship of the relativistic Compton cross section to the electron's velocity distribution. Physical Review B 9, 3237–3241.

Felsteiner, J., Fox, R., Kahane, S., 1970. Compton profile anisotropy in graphite. Physics Letters A 33, 442–443.

Heda, N.L., Dashora, A., Marwal, A., *et al.*, 2010. Electronic properties and Compton profiles of molybdenum dichalcogenides. Journal of Physics and Chemistry of Solids 71, 187–193.

Holt, R.S., Cooper, M.J., Dubard, J.L., *et al.*, 1979. A 412 keV spectrometer for Compton scattering studies. Journal of Physics E: Scientific Instruments 12, 1148–1152.

Jablonska, K.L., Minni, E., Pelka, J., Suoninen, E., Auleytner, J., 1984. XPS and XES study of the valence band of Cr-Al B.C.C. solid solutions scattering. Physica Status Solidi B 123, 627–634.

Lipps, F.W., Tolhoek, H.A., 1954. Polarization phenomena of electrons and photons I: General method and application to Compton scattering. Physica 20, 85–98.

Loupias, G., Petiau, J., 1980. Anisotropic Compton scattering in LiF using synchrotron radiation. Journal de Physique (Paris) 41, 265–271.

Lovesey, S.W., Collins, S.P., 1995. X-ray Scattering and Absorption by Magnetic Materials. New York: Oxford Science Publications, Oxford University Press.

Manninen, S., Paakkari, T., 1978. A high intensity apparatus for accurate Compton profile measurements. Nuclear Instruments and Methods 155, 115–119.

Platzman, P.M., Tzoar, N., 1970. Magnetic scattering of X-rays from electrons in molecules and solids. Physical Review B 2, 3556–3559.

Ribberfors, R., 1975a. Relationship of the relativistic Compton cross section to the momentum distribution of bound electron states. Physical Review B 12, 2067–2074.

Ribberfors, R., 1975b. Relationship of the relativistic Compton cross section to the momentum distribution of bound electron states. II. Effects of anisotropy and polarization. Physical Review B 12, 3136–3141 (1975).

Sakai, N., Ono, K., 1976. Compton profile due to magnetic electrons in ferromagnetic iron measured with circularly polarized γ rays. Physical Review Letters 37, 351–353.

Schülke, W., 2007. Electron Dynamics by Inelastic X-ray Scattering. New York: Oxford Science Publications, Oxford University Press.

Shiotani, N., Sakai, N., Itoh, F., *et al.*, 1989. An X-ray spectrometer for Compton scattering experiments with synchrotron radiation. Nuclear Instruments and Methods in Physics Research Section A 275, 447–452.

Williams, B., 1977. Compton Scattering. London: McGraw-Hill.